

Open-circuit voltage degradation and trap-assisted tunneling in electron and proton-irradiated ultra-thin GaAs solar cells

Cite as: J. Appl. Phys. 135, 224505 (2024); doi: 10.1063/5.0205238

Submitted: 25 February 2024 · Accepted: 21 May 2024 ·

Published Online: 13 June 2024



A. Barthel,^{1,2} S.-I. Sato,³ L. Sayre,¹ J. Li,² T. Nakamura,⁴ T. Ohshima,³ M. Imaizumi,^{4,5} and L. C. Hirst^{1,2,a)}

AFFILIATIONS

¹Department of Materials Science and Metallurgy, University of Cambridge, Cambridge CB3 0FS, United Kingdom

²Department of Physics, University of Cambridge, Cambridge CB3 0HE, United Kingdom

³National Institutes for Quantum Science and Technology (QST), Takasaki, Gunma 370-1292, Japan

⁴Japan Aerospace Exploration Agency (JAXA), Tsukuba, Ibaraki 305-8505, Japan

⁵Faculty of Engineering, Sanjo City University, Sanjo City, Niigata 955-0091, Japan

Note: This paper is part of the special topic, Defects in Semiconductors 2024.

a) Author to whom correspondence should be addressed: lh619@cam.ac.uk

ABSTRACT

Ultra-thin solar cells display high intrinsic radiation tolerance, making them interesting for space applications. This study investigates the dependence of the open-circuit voltage degradation and overall current–voltage behavior of devices with 80 nm thick GaAs absorber layers, on their absorber layer doping concentration and the radiation type used to introduce damage. The radiation types used were 1 MeV electrons and 20 keV, 100 keV, and 1 MeV protons. It is shown that the open-circuit voltage degradation rate increases with absorber layer doping concentration. This is linked to the increase in trap-assisted tunneling enhancement of the recombination rate, facilitated by the increase in electric field strength in the absorber layer with doping concentration. Trap-assisted tunneling is also found to contribute to the high local ideality factors observed in these devices, exceeding values of 2, and to be responsible for the trend of an increasing ideality factor with doping concentration. The significant role of trap-assisted tunneling in the devices is established through fitting of dark current–voltage data using a custom recombination–generation model. An open-circuit voltage degradation rate and local ideality factor curves are also shown to vary with radiation type, despite accounting for their differences in non-ionizing energy loss. This is corroborated by corresponding trends in carrier lifetime damage constants, extracted from the fitting of the dark current–voltage curves. This suggests that the introduction or behavior of radiation damage differs between ultra-thin and conventional, thicker solar cells, where non-ionizing energy loss theory tends to be reliable, especially over the studied proton energy range.

© 2024 Author(s). All article content, except where otherwise noted, is licensed under a Creative Commons Attribution (CC BY) license (<https://creativecommons.org/licenses/by/4.0/>). <https://doi.org/10.1063/5.0205238>

I. INTRODUCTION

Ultra-thin solar cells (UTSCs) are of interest for space applications due to their high intrinsic radiation tolerance. This is manifested in the lack of degradation in the short circuit current (J_{sc}) of these devices up to high radiation doses, orders of magnitude greater than those at which conventional, thicker cells would begin to degrade.^{1,2} As a result, the overall irradiation-induced degradation in device performance of UTSCs is dominated by the

degradation of the open-circuit voltage (V_{oc}). A strong understanding of this V_{oc} degradation and the factors affecting its rate are, therefore, essential for predicting the radiation tolerance of UTSCs and for device optimization.

While the radiation-degradation of solar cells has been studied extensively, the majority of studies have focused on devices, which are orders of magnitude thicker than UTSCs.^{3–8} The conventional models for describing the variation of solar cell parameters with

23 June 2024 13:28:49

irradiation^{9–11} may not all be applicable to UTSCs. For example, UTSCs have already been shown to display unique J_{sc} degradation behavior, which has been linked to the full depletion of absorber layers and the strong electric fields across them in these devices.² Radiation-damaged UTSCs have also been found to display unusual dark current–voltage (DIV) behavior, with ideality factors (η) that exceed a value of 2 and tend to increase with radiation dose;^{1,2} in thicker devices, $1 < \eta < 2$ are usually observed.^{1,5,12,13} It has been suggested that this behavior may also stem from the strong electric field across the absorber layer, which could enable trap-assisted tunneling (TAT) in these devices, leading to the elevated ideality factors.^{14–17}

With the observation of these dissimilarities between the behaviors of UTSCs and thicker devices and the known dependency of V_{oc} on J_{sc} and DIV behavior, it might be expected that the V_{oc} degradation behavior of UTSCs and its dependence on material, device and radiation parameters will differ from that of thicker devices. Previous work by Hirst *et al.* observed little variation in the V_{oc} degradation rate with absorber layer thickness.¹ However, devices with only one absorber layer doping concentration, irradiated with a single type of radiation, were considered. In the present study, the effects of varying these parameters on the V_{oc} degradation rate and DIV behavior of an UTSC design are explored.

UTSCs with an 80 nm thick GaAs homojunction absorber layer, doped to either 1×10^{17} or $1 \times 10^{18} \text{ cm}^{-3}$, were studied. Using a high doping concentration for both the n and p-type absorber layers is of interest for UTSCs, where the short-circuit current is less dependent on diffusion length, compared with conventional thicker cells,^{1,2} and the enhanced built-in voltage from high doping concentration is expected to offer improved carrier separation, carrier extraction, and surface passivation.^{18–20}

The devices were subjected to 1 MeV electron and 20 keV, 100 keV, and 1 MeV proton irradiation to a range of doses. Dark and light current–voltage characterization of the devices was carried out before and after radiation. This revealed that the V_{oc} degradation rate increases with doping concentration. Furthermore, the degradation rate was greater for proton than electron radiation and increased with proton energy, despite using displacement damage dose (DDD) to account for differences in the non-ionizing energy loss (NIEL). DDD and NIEL are measures of the energy deposited by radiation in the target material by atomic displacements, and for conventional, thicker solar cells, they have been successful tools for predicting the variation in the rate of solar cell performance degradation with radiation energy and (to a lesser extent) particle type.^{9,21–23}

To unpick and understand the observed trends in V_{oc} degradation, the DIV curves of the devices were fitted using a dark current model based on Shockley–Read–Hall (SRH) recombination statistics, modified to include the effect of TAT. The results of this fitting were correlated with the observed trends in the V_{oc} degradation rate. This demonstrated that TAT contributes to the elevation of ideality factors in these devices and accounts for the observed increase in the ideality factor and the V_{oc} degradation rate with absorber layer doping concentration. It also allowed the lifetime damage constants to be extracted for 20 and 100 keV proton-irradiated devices, which showed that the increase in the V_{oc} degradation rate with proton energy corresponds with an

increase in the lifetime damage constant. While the model was able to provide explanations for several of the observed trends, it was found to have limitations. In particular, it was found that it did not describe the DIV data for 1 MeV proton-irradiated devices due to their excessively high ideality factors.

The details of these results, their implications, and related discussion are given in Sec. IV. This is preceded by Sec. II on the methods and materials used in the study and Sec. III on the model used to fit the DIV data. The work is concluded with a reiteration of the key results in Sec. V. Supporting details, figure, results, and discussions can be found in the [supplementary material](#).

II. METHODS AND MATERIALS

A. Samples

The UTSCs studied in this work are based around an 80 nm thick GaAs absorber/active layer, which has been shown to offer excellent radiation tolerance.^{1,2} Two device types are considered in this work. They have the same semiconductor layer structure, given in Table I, but are distinguished by the doping concentration used in the GaAs absorber. The doping concentrations are $1 \times 10^{17} \text{ cm}^{-3}$ and $1 \times 10^{18} \text{ cm}^{-3}$.

The BOL performance of both device types is very similar, as demonstrated by Table II. The efficiency of these devices is limited by high transmission losses, which can be mitigated very effectively by light management, without altering the structure of the junction.^{18,24–26}

Further details on the device structure and a description of device fabrication are given in Sec. I A of the [supplementary material](#).

B. Irradiations

The parameters of the exposures carried out are summarized in Table III, with further details on irradiation conditions given in Sec. I B of the [supplementary material](#).

The sets of fluences for each radiation type were chosen to have equivalent values of displacement damage dose (DDD) for unshielded GaAs, with smaller sets for the lower proton energies,

TABLE I. Ultra-thin device layer structure with nominal doping density and thickness values. For the 1×10^{17} devices $x = 1 \times 10^{17}$ and for the 1×10^{18} devices $x = 1 \times 10^{18}$. The n-type contact layer is only present under the front contact metalization (i.e., grid fingers), covering 10% of the mesa area.

Layer function	Material	Dopant	Doping density (cm^{-3})	Thickness (nm)
n-type contact	GaAs	Si	5×10^{18}	300
Hole barrier	$\text{In}_{0.47}\text{AlP}$	Si	5×10^{18}	20
n-type absorber	GaAs	Si	x	40
p-type absorber	GaAs	Be	x	40
Electron barrier	$\text{In}_{0.49}\text{GaP}$	Be	5×10^{18}	20
p-type contact	GaAs	Be	1×10^{19}	25
Etch stop layer	InAlP	Be		150
Substrate	p-GaAs			

23 June 2024 13:28:49

TABLE II. Beginning of life (BOL) performance of ultra-thin solar cells.

Device type	V_{oc} (V)	J_{sc} (mA cm ⁻²)	AM0 efficiency (%)
1×10^{17}	0.971 ± 0.005	9.64 ± 0.10	5.42 ± 0.10
1×10^{18}	0.957 ± 0.007	9.70 ± 0.06	5.33 ± 0.07

due to a limited number of available samples. DDD is a measure of the extent of irradiation, of a material, that has been corrected for the non-ionizing energy loss (NIEL) of the radiation type used.^{22,23} NIEL was calculated using the INFN SR-NIEL calculator in SPENVIS,²⁷ using a threshold displacement energy of 15 eV.²⁸ However, shielding calculations, carried out using MULASSIS²⁹ and the nominal layer thicknesses in Table I, showed that the lower energy protons, in particular, 20 keV protons, experience significant slowing as they pass through the structure. As a result, the DDD is non-uniform and increases with depth, which is shown in Fig. 1 of the [supplementary material](#) (Sec. IB1 in the [supplementary material](#)). The values of DDD for 20 keV protons, and to a much lesser extent 100 keV protons, in Table III, therefore, underestimate the actual amount of displacement damage in the structure for the corresponding fluences. Due to the non-uniformity of DDD with depth, it is difficult to define a single, adjusted DDD value, which is representative of the damage throughout the absorber layer. Rather than attempt this, the unshielded DDD values in Table III are used throughout this study to allow comparisons between the effects of different radiation types to be made. It is worth noting that even the greatest deviation of depth-dependent DDD from the unshielded DDD values, which occurs at the back of the GaAs absorber layer for incident 20 keV protons, is less than half an order of magnitude. This deviation is small for radiation testing of solar cells based on III-V materials, given that the radiation-degradation of device performance parameters is generally found to be proportional to the logarithm of radiation dose, after the onset of degradation.^{10,11}

TABLE III. Summary of radiation testing parameters. DDD is for unshielded GaAs.

Particle type	Energy	DDD (MeV g ⁻¹)	Fluence (cm ⁻²)	Beam flux (cm ⁻² s ⁻¹)
Electrons	1 MeV	6×10^8	3.6×10^{13}	3.1×10^{11}
		6×10^9	3.6×10^{14}	3.1×10^{12}
		6×10^{10}	3.6×10^{15}	3.1×10^{12}
		6×10^{11}	3.6×10^{16}	3.1×10^{12}
Protons	20 keV	6×10^9	6.3×10^9	1.0×10^8
		6×10^{11}	6.3×10^{11}	9.0×10^8
	100 keV	6×10^9	1.8×10^{10}	1.4×10^9
		6×10^{11}	1.8×10^{12}	1.7×10^{10}
	1 MeV	6×10^8	1.2×10^{10}	6.0×10^8
		6×10^9	1.2×10^{11}	6.0×10^8
		6×10^{10}	1.2×10^{12}	7.6×10^9
		6×10^{11}	1.2×10^{13}	2.8×10^{10}

C. Electrical characterization

Dark IV (DIV) and light IV (LIV) measurements of the UTSCs were carried out at room temperature before and after irradiation. An AM0 spectrum was used for LIV, and the key parameters extracted were open-circuit voltage (V_{oc}) and short-circuit current (I_{sc}). The DIV data was analyzed by calculating the local ideality factor, $\eta(V)$, and by fitting the DIV curves using the model described in Sec. III.

$\eta(V)$ is a useful metric for the analysis of DIV data as it can be used to identify the recombination mechanisms operating in the junction at different biases. It is defined as

$$\eta(V) = \frac{q}{kT} \left[\frac{d \ln J}{dV} \right]^{-1}, \quad (1)$$

where V is the applied voltage, J is the current density, and q , k , and T are elemental charge, the Boltzmann constant, and temperature, respectively.

A local ideality factor close to a value of 2 is usually indicative of recombination in the depletion region.^{5,13}

D. Simulation of band structure

To facilitate the fitting of DIV data using the model introduced in Sec. III, simulations of the band structure, including the electric potential and field across the UTSC structure, were required. These simulations were carried out using the Poisson-drift-diffusion (PDD) equation solver of Solcore, which is an open source, Python-based semiconductor modeling package developed predominantly by Alonso-Álvarez *et al.*³⁰

III. FITTING CURRENT-VOLTAGE CURVES

The DIV curve of a device contains a wealth of information about the properties of the device and the materials comprising it. This information can be extracted by fitting the data with an appropriate model. The fitting model used in this study builds on classical Shockley-Read-Hall (SRH) recombination statistics, integrating a model for trap-assisted tunneling, which is hypothesized to affect the recombination in the presence of a substantial electric field, as found in the depletion regions of the ultra-thin solar cells.

The current in the ultra-thin solar cells is expected to be dominated by recombination-generation current, rather than diffusion, because the absorber layers of the cells are fully depleted, with their depletion regions spanning their active layers. This is demonstrated by Fig. 1, which shows a non-zero electric field across the absorber layer for both device types. The recombination-generation current density, J_{rg} , is obtained by integrating the carrier recombination rate (U), with respect to position (x), over the entire width of the depletion region, represented by W in the integral,

$$J_{rg} = q \int_W U dx. \quad (2)$$

SRH recombination statistics give the following expression for the recombination rate in the depletion region, the derivation of

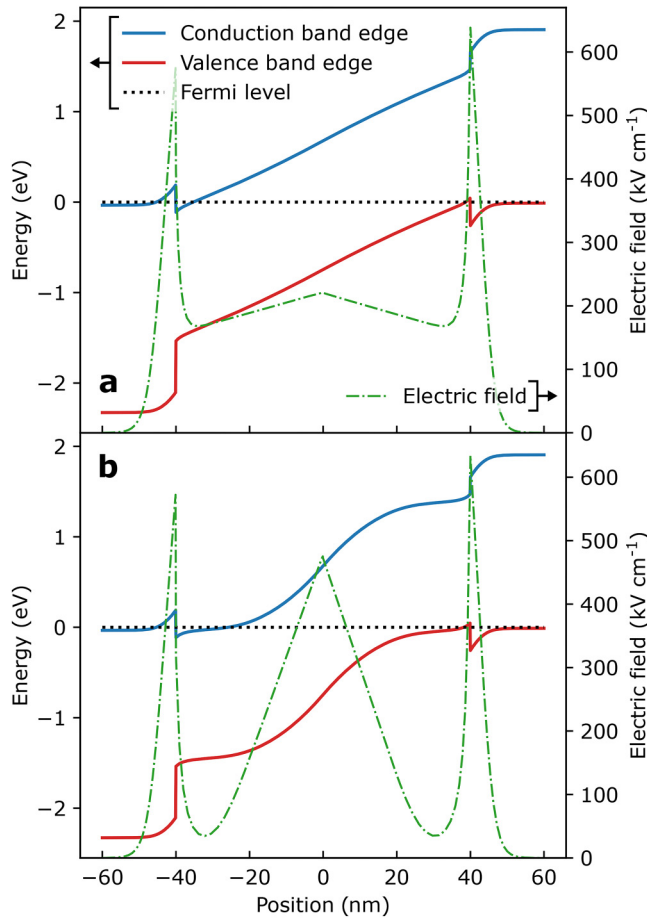


FIG. 1. Equilibrium band structures for (a) 1×10^{17} and (b) 1×10^{18} devices are shown, including the passivation layers at either end and the GaAs absorber in the middle. The conduction and valence band edges are shown, alongside the Fermi level and the electric field across the junction. These were calculated using the Solcore PDD calculator.³⁰

which can be found elsewhere,^{5,13}

$$U = \frac{\frac{n_i}{\sqrt{\tau_p \tau_n}} \sinh\left(\frac{qV_j}{2kT}\right)}{\cosh\left(\frac{E_{F0} - E_i}{kT} + \ln\sqrt{\frac{\tau_p}{\tau_n}}\right) + \exp\left(-\frac{qV_j}{2kT}\right) \cosh\left(\frac{E_t - E_i}{kT} + \ln\sqrt{\frac{\tau_p}{\tau_n}}\right)} \quad (3)$$

$E_{F0} = \frac{1}{2}(E_{Fn} + E_{Fp})$ and $V_j = \frac{1}{q}(E_{Fn} - E_{Fp})$. V_j is the voltage across the junction due to the applied bias. τ_n and τ_p are the minority electron and hole carrier lifetimes, respectively. n_i is the intrinsic carrier concentration, E_i is the intrinsic Fermi level, and E_t is the trap energy level. As is made clear later, $E_t - E_i$ is an important variable in determining the recombination rate and it is commonly abbreviated as ΔE_t .

This expression only considers a single defect energy level (ΔE_t) in the bandgap of the active layer. However, multiple different defects may be present. Deep level transient spectroscopy (DLTS) of radiation damaged devices has shown that electron and proton radiation introduce several different types of defects into semiconductors with different energy levels.^{31–34} As long as the defects do not interact, which is expected to be a reasonable assumption at low defect densities, they can be considered parallel circuit elements and the total current is simply the sum of the individual recombination-generation currents from each defect level (d),⁵

$$J_{rg} = \sum_d q \int_w U_d dx. \quad (4)$$

A. Trap-assisted tunneling

Trap-assisted tunneling (TAT) is an alternative recombination process to SRH recombination, which relies on the presence of a strong electric field in the junction. Due to the electric field and associated band-bending, the quantum mechanical carrier wavefunctions can extend into the forbidden gap of the semiconductor. Therefore, if there are defect states present in the bandgap, a finite probability exists that carriers will tunnel from the band edges into the defect states. A combined process of tunneling and thermionic capture may also take place.^{35–38} A schematic of this process is shown in the [supplementary material](#) (Sec. II A, Fig. 2), which also explains the strong dependence of TAT on electric field strength. TAT may be considered to be an enhancement of SRH recombination, with tunneling allowing carriers with a wider range of energies to be captured by a defect, but the two-stage process of capturing a carrier of each type still being required for recombination.

The effect of trap-assisted tunneling (TAT) on the recombination-generation current is included in the model from Sec. III using the formalism developed by Hurkx *et al.* The full derivation of this theory is available elsewhere,³⁸ and only the key results are reproduced here.

The theory suggests that TAT modifies the carrier lifetimes in Eq. (3) through a pair of enhancement factors (Γ_n and Γ_p). The subscripts n and p indicate whether quantities pertain to electrons or holes, respectively. τ_{n0} and τ_{p0} are the minority carrier lifetimes in the absence of an electric field,

$$\tau_n = \frac{\tau_{n0}}{\Gamma_n + 1}, \quad (5)$$

$$\tau_p = \frac{\tau_{p0}}{\Gamma_p + 1}. \quad (6)$$

$\Gamma_{n,p}$ is given by

$$\Gamma_{n,p} = \frac{\Delta E_{n,p}}{kT} \int_0^1 \exp\left[\frac{\Delta E_{n,p}}{kT} u - K_{n,p} u^{\frac{3}{2}}\right] du, \quad (7)$$

23 June 2024 13:28:49

where

$$K_{n,p} = \frac{4}{3} \frac{\sqrt{2m_{n,p}^* \Delta E_{n,p}^3}}{q\hbar|F|}. \quad (8)$$

$\Delta E_{n,p}$ is the difference in energy between the conduction band edge and the defect level (ΔE_n) or the defect level and the valence band edge (ΔE_p). $m_{n,p}^*$ is the effective mass of the relevant carrier, F is the local electric field, and \hbar is the reduced Planck's constant.

TAT effectively decreases the carrier lifetime, which results in an increase in the recombination-generation rate and current. The enhancement factors, $\Gamma_{n,p}$, increase monotonically with electric field, from a minimum value of 0 in the absence of an electric field. Therefore, TAT enhancement of the recombination-generation current is expected to increase monotonically with electric field strength. Figure 2 shows the variation of the electric field strength at the n-p junction interface (F_{\max}) of the 1×10^{17} and 1×10^{18} devices with an applied bias, calculated using the Solcore PDD calculator. For plots of the spatial variation of electric potential and field $[F(x)]$ in the absorber layer at different applied biases, see Fig. 3 in the [supplementary material](#). The electric field is stronger in the 1×10^{18} devices and varies more with an applied bias than in the 1×10^{17} devices, leading to the same trends in the TAT enhancement factor, as seen in Fig. 4 of the [supplementary material](#). The variation of electric field with an applied bias in these ultra-thin devices differs from that expected for a conventional, thick n-p homojunction, as the depletion region width is limited by the highly doped passivation layers bounding the ultra-thin absorber layer.

$\Gamma_{n,p}$ also has a strong dependence on the carrier effective mass. A consequence of this is that TAT enhances the trapping rate

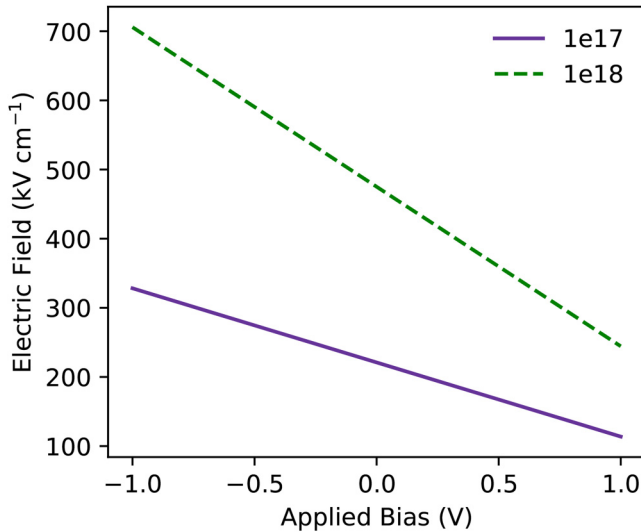


FIG. 2. The electric field at the n-p interface (i.e., position = 0 nm) is plotted against the applied bias for 1×10^{17} and 1×10^{18} devices. The electric field was calculated using the Solcore PDD calculator.

of light holes (lh) more than that of heavy holes (hh), which can be seen in Fig. 4 of the [supplementary material](#), showing plots of the TAT enhancement factor for different carrier types. As a result, the contribution of light holes to the total recombination rate will be significantly greater than in the absence of an electric field, where it is generally small due to their low intrinsic concentration. Recombination-generation processes involving the two hole types are expected to take place in parallel, without interfering with each other, and therefore, their recombination-generation rates are summed to give the total rate,

$$U_d = U_{d,lh} + U_{d,hh}. \quad (9)$$

The effect of TAT on the recombination-generation current and the associated local ideality factor for a 1×10^{18} device with a single defect level in the center of the bandgap is demonstrated in Fig. 3. The figure shows curves for J_{rg} including and neglecting the effect of TAT. The contributions of light and heavy holes are given separately, along with their combined total. It is clear in Fig. 3(a) that TAT enhances J_{rg} and that it does so to different extents for recombination involving light and heavy holes. The enhancement decreases with increasing voltage since the electric field strength decreases such that the TAT-SRH curves tend toward the basic SRH curves. This leads to a key characteristic of TAT-SRH, which is an elevated ideality factor, as seen in Fig. 3(b). On their own, SRH recombination statistics predict that $\eta(V)$ will not exceed a value of 2. Higher values can be observed if shunting and/or series resistance are active, but these effects are confined to particular current ranges and, therefore, also voltage ranges. However, with TAT-SRH, $\eta(V) > 2$ is expected over a wide voltage range, including the intermediate forward bias range, where shunting and series resistance are usually negligible.

The effect of series resistance (R_s) can also be included in the model by using an effective voltage across the junction, $V_j = V - JR_s$, where V is the applied voltage.

B. Fitting considerations

An aim of this study is to fit DIV data with the model for recombination-generation current introduced above. To facilitate its integration into an efficient fitting algorithm, it is advantageous to make some approximations. The main approximations are

- (a) Exponential spatial variation in the recombination rate across the junction and (b) position-independent TAT enhancement factor, which allow the recombination rate in forward bias to be integrated analytically. (a) is expected in the forward bias when approximating the spatial variation in the electric potential as linear.
- Low-field approximation for the TAT enhancement factor, which simplifies the expression for $\Gamma_{n,p}$.

Details of these approximations are given in Sec. II B of the [supplementary material](#), and their impact on the accuracy of the model is discussed below.

Several variations of a recombination-generation current model based on SRH recombination statistics have been introduced in this section. In order to clarify which models are used

23 June 2024 13:28:49

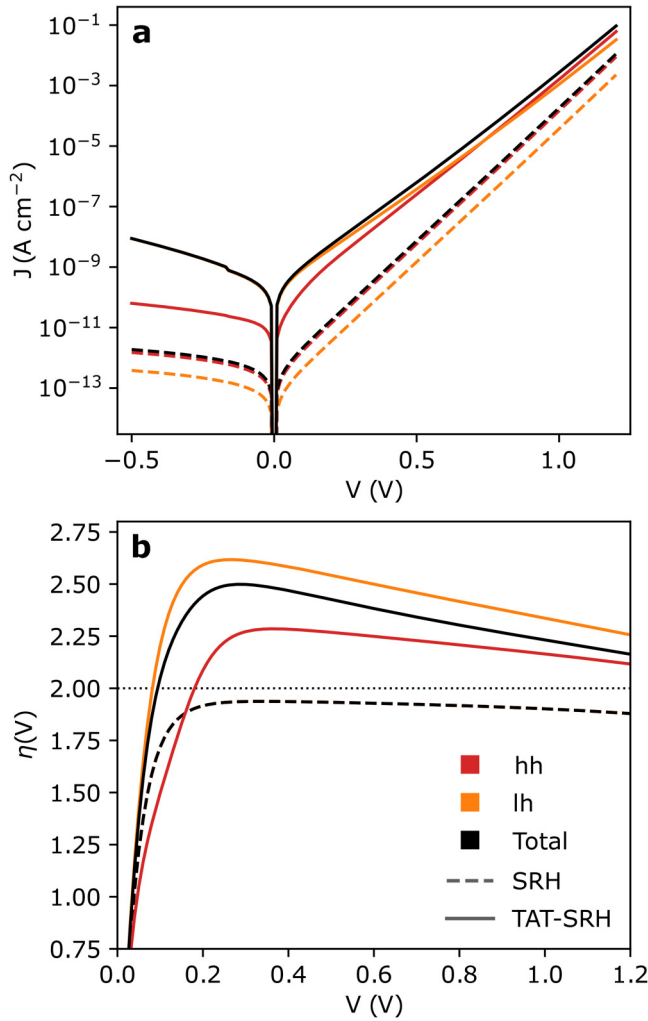


FIG. 3. (a) Recombination-generation current (J) and (b) local ideality factor [$\eta(V)$] for a 1×10^{18} device with a defect level at $\Delta E_i = 0$, calculated with (TAT-SRH) and without (SRH) incorporating TAT enhancement, are plotted as functions of voltage. The total recombination current is given, along with the separate contributions from recombination-generation involving heavy holes (hh) and light holes (lh). In the case where TAT is not included (SRH), the hh, lh, and total $\eta(V)$ curves overlap. In (a), the kink in the TAT-SRH curves, at a low reverse bias between -0.2 and -0.1 V, is a result of an artifact in the Solcore PDD calculator, which causes discontinuity in the variation of potential with an applied bias.

throughout Secs. III B 1 and III B 2, a summary of these variants is given in Table IV.

Another consideration for fitting real data is that of different defect types. In this study, the concept of a *broad defect* is used to fit some features in the data. This is also discussed in this section.

1. Impact of approximations

The impact of these approximations on the accuracy of the model is considered in Fig. 4. Panel (a) depicts current-voltage

TABLE IV. Summary of recombination-generation current model variants used in this work.

Model name	Description
SRH	Eqs. (3), (4), and (9); $E_i(x)$, $F(x)$ from PDD
SRH-A	SRH + Approx. 1(a); F_{\max} from PDD
TAT-SRH	SRH + Eqs. (5)–(8); $E_i(x)$, $F(x)$ from PDD
TAT-SRH-A	TAT-SRH + Approx. 1 and 2; F_{\max} from PDD

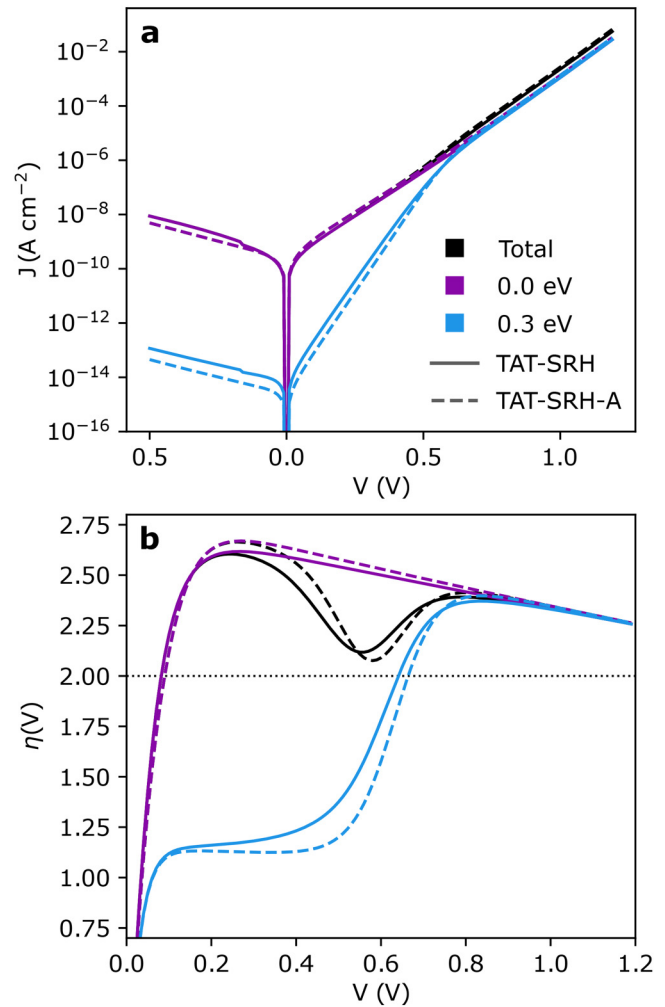


FIG. 4. (a) Recombination-generation current and (b) the associated local ideality factor are plotted for 1×10^{18} devices with two defect levels (ΔE_i), at 0.0 and 0.3 eV, using the TAT-SRH and TAT-SRH-A models. The total current as well as the contributions of the individual defect levels are shown.

23 June 2024 13:28:49

curves for a 1×10^{18} device with defect levels (ΔE_t) at 0.0 and 0.3 eV, calculated using both TAT-SRH and TAT-SRH-A. The contributions from the individual defect levels are shown, alongside their summed total. The local ideality factor is shown in panel (b). Figure 4(a) demonstrates that the greatest deviation between TAT-SRH and TAT-SRH-A occurs in the reverse bias regime, where the approximations used in TAT-SRH-A break down. It also shows that the contribution of the off-center 0.3 eV defect level is insignificant until a forward bias of ~ 0.6 V is reached. The reason for this is that the defect only becomes an effective recombination center once the electron quasi-Fermi level exceeds the defect energy level. The additional current from the off-center defect causes a slight increase in the slope in the DIV curve near this *transition voltage*, causing the local trough in the $\eta(V)$.⁵ The approximate model (TAT-SRH-A) replicates this feature well (see Fig. 4), although the deviation from TAT-SRH is more noticeable in $\eta(V)$, than in the DIV.

The fitting parameters of the TAT-SRH-A model are the number of defects, the energy levels of the defects (ΔE_t), the carrier lifetime for the defects ($\tau_0 = \tau_{n0} = \tau_{p0}$), and the series resistance (R_s). Changing the ratio of τ_{n0} to τ_{p0} affects the shape of the DIV and $\eta(V)$ curves in a similar manner to changing the position of the defect energy levels. Both variables can shift the position of troughs in $\eta(V)$, and their effects are difficult to distinguish. In fitting, this increases the number of local optima in the parameter space and reduces the likelihood and rate of convergence to a unique solution. To avoid these issues, the ratio is set to 1 such that $\tau_{n0} = \tau_{p0}$. The consequences of this are evaluated in Sec. III B 1 of the [supplementary material](#).

2. Broad defects

Finally, in the cases where broad troughs are present in the $\eta(V)$ curves, the data may not be fit efficiently by defects with single delta-function-like (δ) energy levels. Using multiple, closely spaced, independent defect levels may yield a good fit, but this requires a large number of free variables to be fit. An alternative is to use the concept of a *broad defect*, which comprises multiple, closely spaced δ -defects that are not independent, but related by a function. In this study, the lifetimes of δ -defects constituting a broad defect are given a Gaussian distribution. As a result, these Gaussian (G) defects can be defined by only three parameters: lifetime (τ_0), peak energy level (ΔE_t), and peak width, given by the standard deviation (S), which is only one more parameter than a δ -defect.

Broad defects also have a physical interpretation, which is that of defect clusters. In defect clusters, many, closely-spaced point defects may interact, causing their energy levels to broaden into a small energy band. Previous studies^{32,39,40} have suggested that proton irradiation can introduce defect clusters in GaAs.

IV. RESULTS AND DISCUSSION

The devices were characterized by means of DIV and LIV, both before and after irradiation. From the LIV data, the short-circuit currents (J_{sc}) and open-circuit voltages (V_{oc}) of the devices were extracted. No degradation in J_{sc} was observed for these devices, regardless of radiation type and dose (see Fig. 5 in the

[supplementary material](#) for a plot of short-circuit current remaining factor against displacement damage dose). This is expected since the previous work on almost identical devices demonstrated that the beginning-of-life (BOL) J_{sc} of the devices is preserved up to a significantly greater dose than the maximum used in this study.²

In contrast, the V_{oc} of the devices does degrade with fluence over the range of doses probed in this study. This is shown in Figs. 5 and 6, where the V_{oc} remaining factor (RF) is plotted against displacement damage dose (DDD) for both device types and all radiation types used. The V_{oc} RF is the ratio of the pre- and post-irradiation V_{oc} of a device. While the data presented by both figures are the same, Fig. 5 highlights differences due to the radiation type, whereas Fig. 6 focuses on differences due to doping

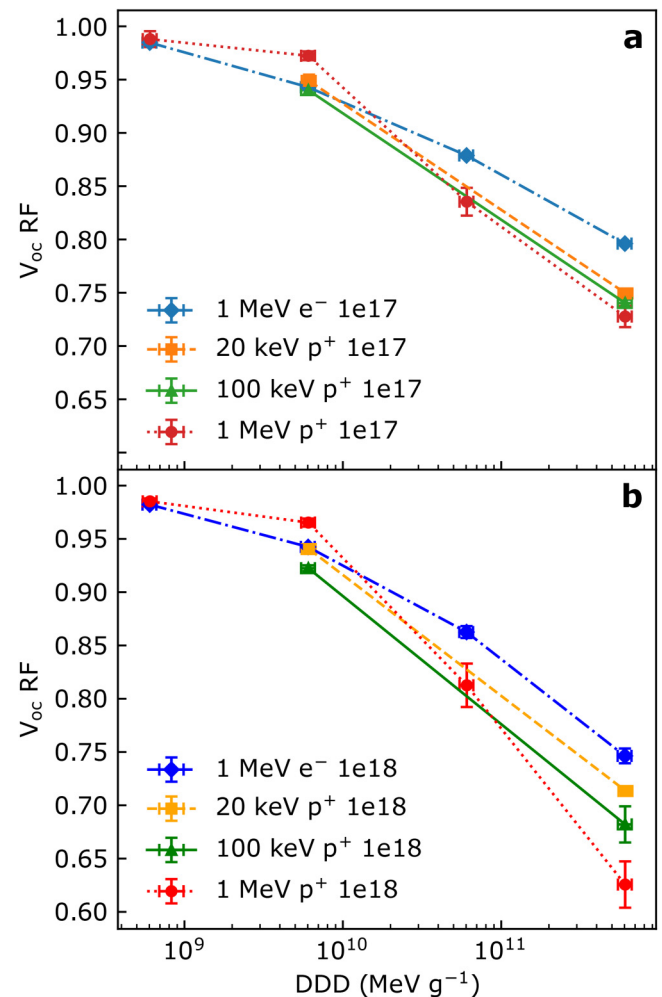


FIG. 5. V_{oc} remaining factor (RF) is plotted against DDD for (a) 1×10^{17} and (b) 1×10^{18} devices irradiated with 1 MeV electrons and 20 keV, 100 keV, and 1 MeV protons. The lines connecting points only function as guides to the eye.

23 June 2024 13:28:49

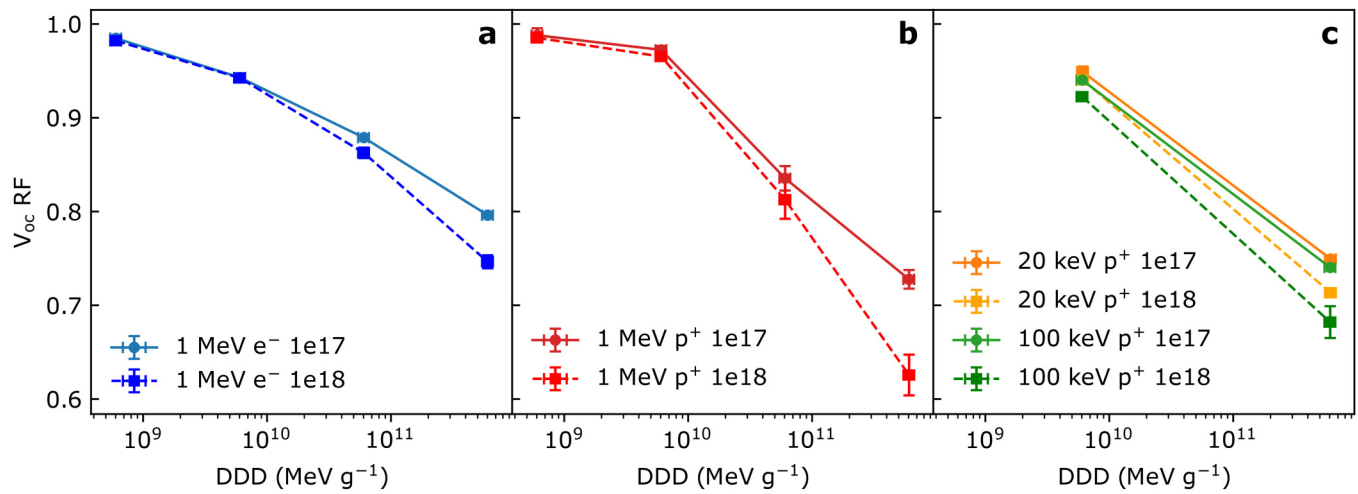


FIG. 6. V_{oc} remaining factor (RF) is plotted against DDD for 1×10^{17} and 1×10^{18} devices irradiated with (a) 1 MeV electrons, (b) 1 MeV protons, and (c) 20 keV and 100 keV protons. The lines connecting points only function as guides to the eye.

concentration. The V_{oc} RF is plotted against DDD, instead of fluence, to account for the difference in the non-ionizing energy loss (NIEL) of the different radiation particle types and energies used. The DDD used here is the unshielded DDD from Table III, which is known to slightly underestimate the true DDD for 100 keV protons and more substantially for 20 keV protons. As a result, the degradation curves for different proton energies are not expected to overlap exactly, but to be slightly shifted relative to each other, while maintaining a similar shape. The shift should be such that the V_{oc} RF decreases with decreasing proton energy. However, the opposite is observed in Fig. 5, with V_{oc} degradation increasing with proton energy. It is also found that the shapes of the degradation curves differ, diverging significantly at the upper end of the DDD range tested and that, for the same DDD, protons cause greater degradation in V_{oc} than 1 MeV electrons. Furthermore, Fig. 6 shows that a clear difference in the degradation rate exists between the 1×10^{17} and 1×10^{18} devices. Regardless of the radiation type, the V_{oc} of the 1×10^{17} devices degrades more slowly than that of the 1×10^{18} devices. It is unlikely that this difference due to doping concentration can be attributed to a significant difference in the pre-irradiation defect density, as this would lead to a difference in the onset of degradation, which is not observed. Instead the onset of degradation seems to be very similar for both device types and the difference in the degradation rate only becomes apparent beyond this onset.

The value of V_{oc} is dependent on both the J_{sc} and the variation of current with voltage in the device. To decouple the latter from the effects of illumination and understand its influence on V_{oc} , DIV measurements were carried out. DIV data were collected for all devices before and after irradiation, except for the devices irradiated with 20 and 100 keV protons, where these measurements were only made post-irradiation, due to time constraints. From the DIV curves, local ideality factor curves can be calculated, using Eq. (1), which emphasize subtle variations in the gradients of the DIV curves.

The full set of DIV $[J(V)]$ and local ideality factor $[\eta(V)]$ curves, for all devices represented in the V_{oc} data in Figs. 5 and 6, is given in Figs. 6 and 7 of the supplementary material. The key features of this data set are summarized in Fig. 7, where the local ideality factor curves are plotted for devices irradiated with different radiation types, grouped by doping concentration and DDD. The local ideality factor is shown, instead of the absolute current, as it highlights differences and trends in the current-voltage behavior more clearly. The main trend that it does not capture is the increase in absolute current at a given voltage (alternatively, reverse saturation current) with the radiation dose, as expected from the radiation-induced introduction of defects into the active region of the device. This trend is depicted in Figs. 6 and 7 of the supplementary material.

The local ideality factor curves in Fig. 7 reveal several other trends. The ideality factor of 1×10^{18} devices is generally greater than that of 1×10^{17} devices and for both device types, $\eta(V) > 2$ for part of the voltage range. $\eta(V)$ tends to increase with the radiation dose, though the extent of this depends on the applied bias, radiation type, and doping density. An exception to this is in the 20 and 100 keV proton irradiated devices at a low forward bias, where $\eta(V)$ decreases with increasing dose. These low energy proton irradiated devices have very similar $\eta(V)$ across the tested voltage range. For 1 MeV proton irradiated devices, the curves are also similar in shape, especially at high DDD, but are shifted to higher values of $\eta(V)$. The curves for 1 MeV electron-irradiated devices are more dissimilar in shape. For example, they include a narrow trough in $\eta(V)$ at high bias, which is not observed for proton-irradiated devices. The subsequent sharp increase in $\eta(V)$ is common to all of the devices and marks the onset of series resistance. The onset of series resistance shifts to lower biases with increasing radiation dose since the reverse saturation current increases. A further common feature, particularly for devices with low reverse saturation current, e.g. pre-irradiation or low dose devices, is the presence of noise at low biases. This is a result of the

23 June 2024 13:28:49

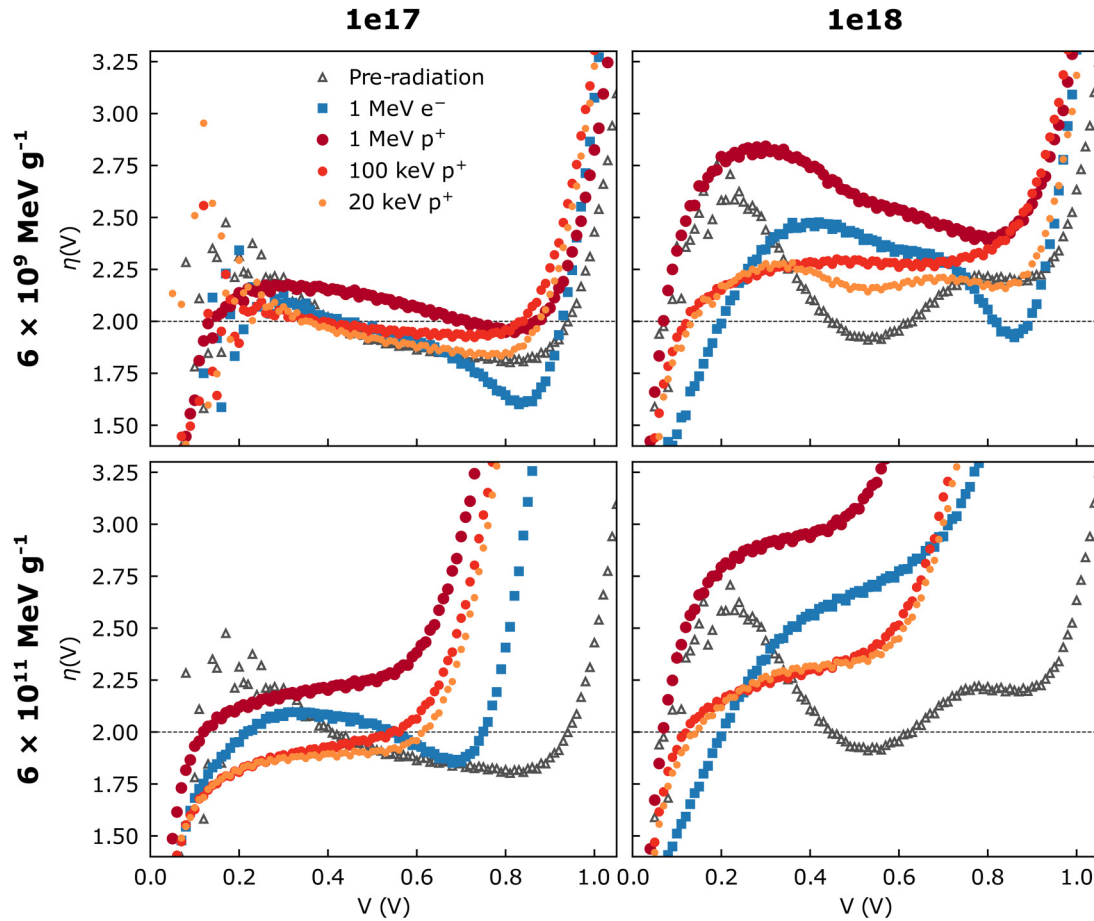


FIG. 7. Local ideality factor, $\eta(V)$, is plotted for 1×10^{17} and 1×10^{18} devices irradiated with 1 MeV electrons and 20 keV, 100 keV and 1 MeV protons to DDD of $6 \times 10^9 \text{ MeV g}^{-1}$ and $6 \times 10^{11} \text{ MeV g}^{-1}$. The key in the top-left panel indicates radiation type and applies to all panels. Data for proton-irradiated devices are represented by red dots, with their size and tone depending on the proton energy: larger and darker dots for higher energy.

low currents being measured, which are close to the noise floor of the measurement setup.

A number of factors can influence the shape and magnitude of local ideality factor curves. Section III discusses some of these factors, mainly trap-assisted tunneling (TAT) and the presence of defects in the bandgap, and establishes models for current-voltage behavior, which take their effects into account: TAT-SRH and TAT-SRH-A.

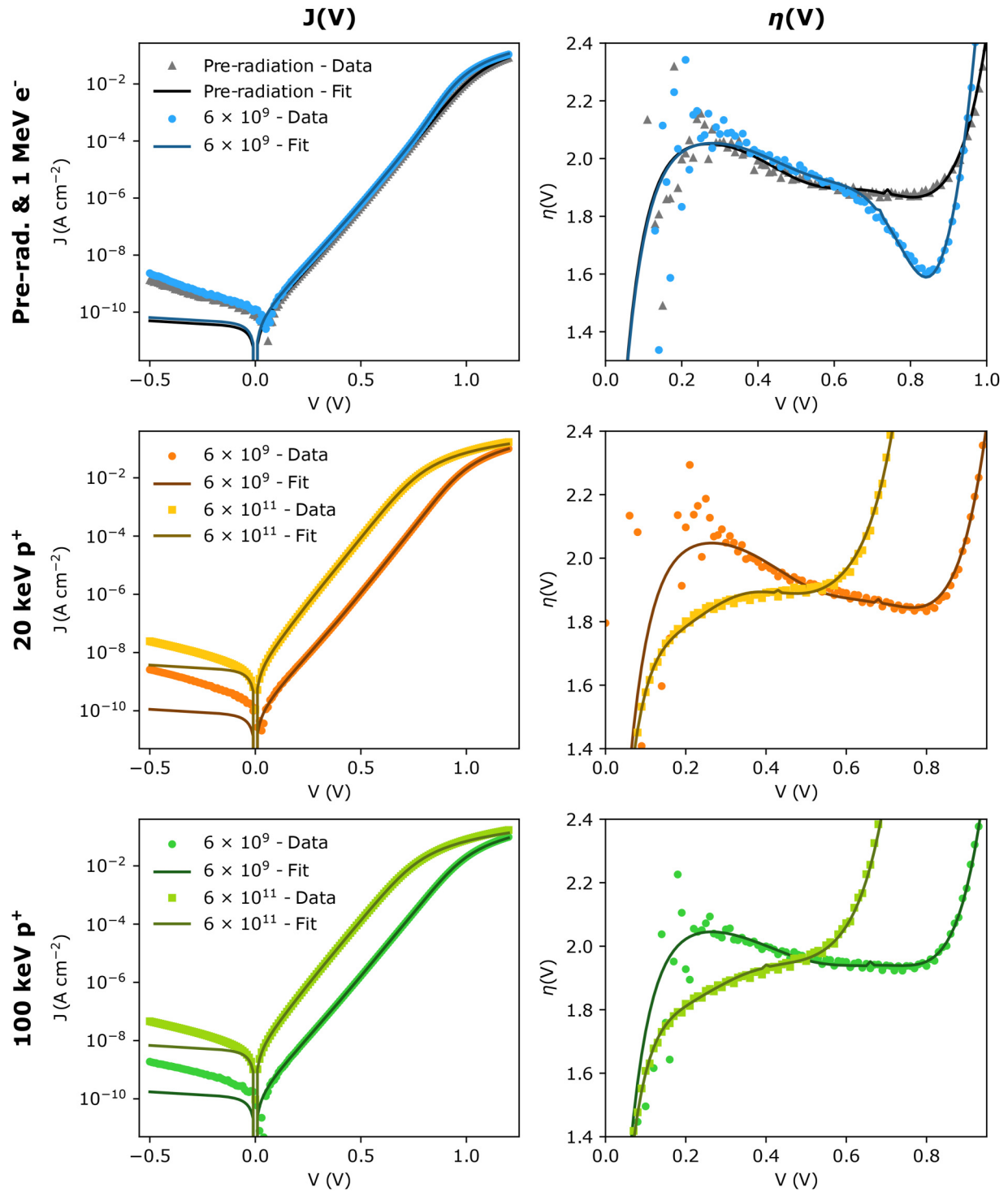
A. DIV fitting

The experimental DIV curves were fitted using the TAT-SRH-A model introduced in Sec. III. The optimization of fitting parameters was handled by a genetic algorithm, which is further discussed in Sec. II C of the [supplementary material](#). The resulting fits to the DIV data, and the associated local ideality factors, are plotted in Figs. 8 and 9 for the 1×10^{17} and 1×10^{18} devices, respectively. The fitting parameters are given in Table 1 of the [supplementary material](#).

Good fits to the data were attained for pre-irradiation, $6 \times 10^9 \text{ MeV g}^{-1}$ 1 MeV electron-irradiated and 20 keV and 100 keV proton-irradiated devices with this model. In the cases of the 1 MeV proton-irradiated devices or high dose 1 MeV electron-irradiated devices, the DIV data could not be fitted well with this model, as the local ideality factors for these devices exceeded the maximum possible ideality factor predicted by the model.

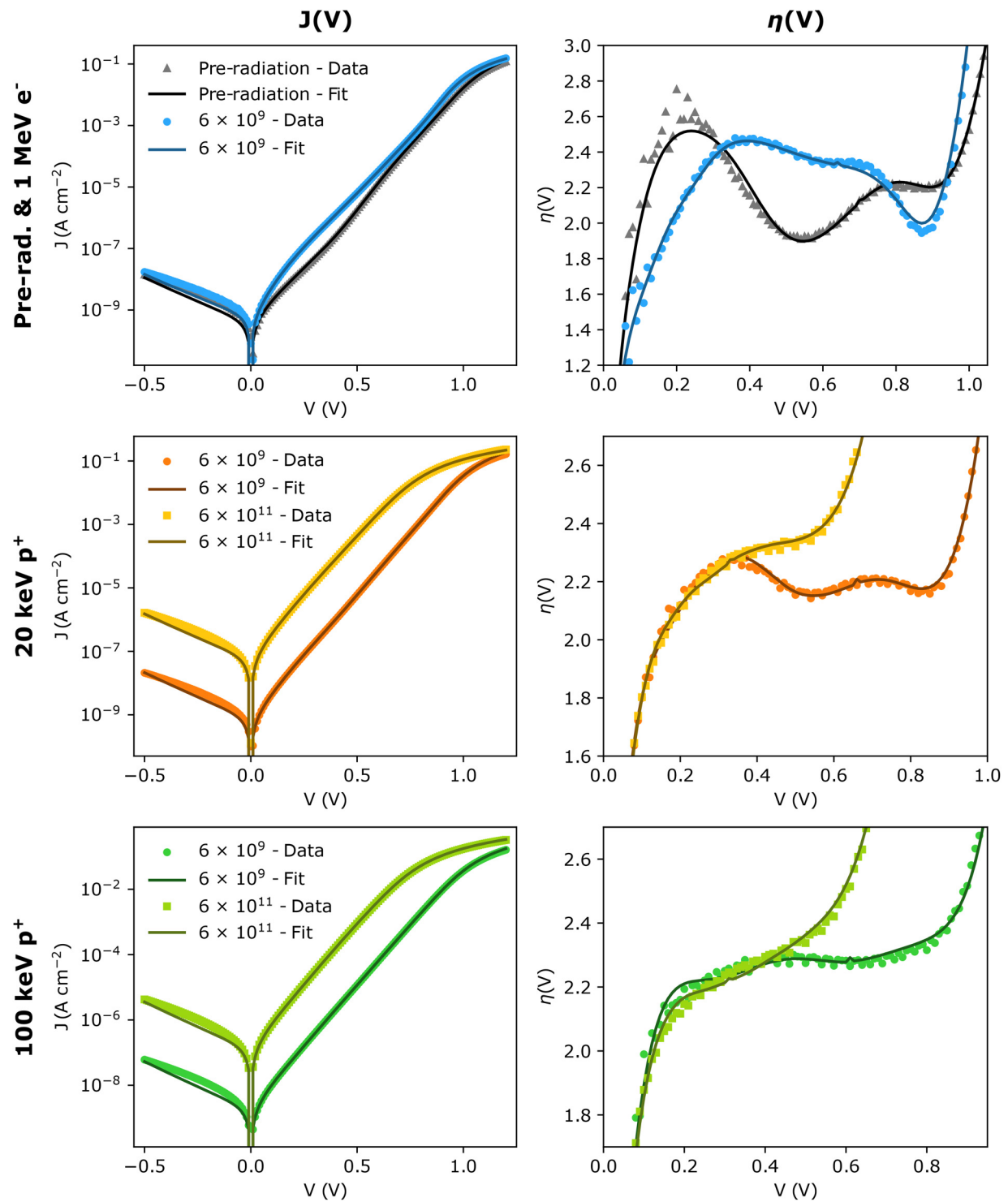
While the DIV, rather than the local ideality factor, was fitted, the latter was crucial for characterizing the quality of a fit. It was also used to decide on the range of data to be fitted, the number of defects to be fitted, and the bounds for the initial guesses for the defect parameters. The local ideality factor is better suited to inform these decisions than the DIV curve because it emphasizes variations in the DIV and its shape and magnitude can be clearly associated with physical traits.

As noted above, a selection was made of the voltage range fitted for each DIV curve, although the plotted fits in Figs. 8 and 9 are extrapolated to the full voltage range of the data. The chosen voltage



23 June 2024 13:28:49

FIG. 8. TAT-SRH-A fits to experimental DIV $[J(V)]$ data for 1×10^{17} devices are shown, along with the associated local ideality factor curves $[\eta(V)]$. Data are shown for a device pre- and post-irradiation with 1 MeV electrons to a DDD of 6×10^9 MeV g⁻¹ in the top panels. In the remaining panels, data are given for 6×10^9 and 6×10^{11} MeV g⁻¹ 20 keV and 100 keV proton-irradiated devices.



23 June 2024 13:28:49

FIG. 9. TAT-SRH-A fits to experimental DIV [$J(V)$] data for 1×10^{18} devices are shown, along with the associated local ideality factor curves [$\eta(V)$]. Data are shown for a device pre- and post-irradiation with 1 MeV electrons to a DDD of 6×10^9 MeV g⁻¹ in the top panels. In the remaining panels, data are given for 6×10^9 and 6×10^{11} MeV g⁻¹ 20 keV and 100 keV proton-irradiated devices.

range only included the forward bias regime since the approximations made for TAT-SRH-A are known to be inaccurate in reverse bias. A discussion of the applicability of the model without the approximations (TAT-SRH) in the reverse bias regime is given in Sec. III A 2 of the [supplementary material](#). Within a forward bias, the lower bound of the voltage range for fitting was chosen to avoid very low currents, at which light biasing is non-negligible. In practice, this could place the lower bound as high as ~ 0.25 V for the devices with the lowest reverse saturation currents. The upper bound was chosen to exclude the very high bias region, where the slope of $\eta(V)$ is very steep, as it is dominated by series resistance. It is very difficult to discern the presence of defects in this region and choose appropriate initial guesses for their parameters. The onset of series resistance was still included in the fitting range.

Figures 8 and 9 show that the fitting model was able to account for the wide variety of $\eta(V)$ curve shapes and magnitudes found across the devices.

The component of the model that allows for $\eta(V) > 2$ is TAT, which is facilitated by the presence of an electric field across the junction. TAT also explains the generally greater $\eta(V)$ for the 1×10^{18} devices since the magnitude of the electric field and its variation with applied bias are greater in the 1×10^{18} devices.

The variations in the $\eta(V)$ shape between devices with the same absorber layer doping concentration, but subjected to different radiation types and doses, are found to result from differences in the sets of defects used to fit the DIV curves, an effect that has been previously observed by Chen *et al.*¹² and Pellegrino *et al.*⁵ This includes differences in the number of defect levels used, their energy levels and widths, as well as the carrier lifetimes associated with carriers being trapped by them. The radiation-induced introduction of various defects with different energy levels in GaAs devices has been demonstrated by DLTS studies, which show that the types and densities of defects introduced can vary with the radiation particle type (e.g. electrons or protons) and radiation energy.^{5,31,32,41}

However, the aim of this study is not to use DIV fitting for the identification of defects, but to use it to understand the variation in the V_{oc} degradation rate with absorber layer doping concentration and radiation type. Identification of defects is not necessary for this purpose. This is reflected in the approach to DIV fitting that was applied, which generally aimed to achieve a good fit with the fewest defects and fitting parameters. A major reason for this approach was the lack of unique solutions in fitting, i.e. the same DIV curve could be fit with alternative defect sets, although the total lifetimes ($\tau_{0,total}$) of these defect sets must be very similar if they give good fits to the DIV curve. $\tau_{0,total}$ for a device corresponds to the total recombination rate in its absorber layer ($\sum_d U_d$) at sufficiently high quasi-Fermi level splitting to activate all the identified defects in that device. For the devices in this study, this condition is met at forward biases corresponding to and greater than the respective V_{oc} values of the devices. The values of $\tau_{0,total}$ extracted from DIV fitting are plotted against DDD in Fig. 10. $\tau_{0,total}$ decreases with increasing DDD, as is expected from the introduction of radiation defects.^{2,41–43} $\tau_{0,total}$ is observed to be consistently greater in the 1×10^{18} devices than in the 1×10^{17} devices. In conventional, thicker devices, this would be expected to lead to greater values of V_{oc} for the 1×10^{18} devices. However, the opposite is observed in this study (see Table II and Fig. 5). This can be attributed to the difference in the TAT

enhancement factor between the two device types, as is discussed further in Sec. IV B 1.

Further discussion of the defect sets used to fit the DIV curves and the approach to fitting can be found in Sec. III A 1 of the [supplementary material](#).

B. Implications of DIV fitting results

The material and device parameters extracted from fitting in Sec. IV A can now be used to understand the effects of (i) doping concentration and (ii) radiation type on V_{oc} degradation, which are illustrated by the V_{oc} remaining factor degradation curves in Figs. 5 and 6.

1. Effect of doping concentration

In fitting the DIV data, there was one main difference between the 1×10^{17} and 1×10^{18} devices, which was in the TAT enhancement. As demonstrated by the magnitudes of local ideality factors in Figs. 7–9, TAT enhancement of the recombination rate is a stronger effect in the 1×10^{18} devices than in the 1×10^{17} devices due to the greater magnitude of and variation in the electric field in the 1×10^{18} devices (see Fig. 2). The TAT enhancement factor reduces the effective carrier lifetime, increasing the reverse saturation current, which causes a decrease in V_{oc} . It is, therefore, reasonable to expect that the greater values of Γ in the 1×10^{18} devices are the cause of their lower values of V_{oc} and greater V_{oc} degradation rate. This hypothesis can be tested by comparing the predicted V_{oc} degradation rate for each device type with and without TAT enhancement. The V_{oc} can be predicted using the principle of superposition⁴⁴ with the measured short-circuit currents and the

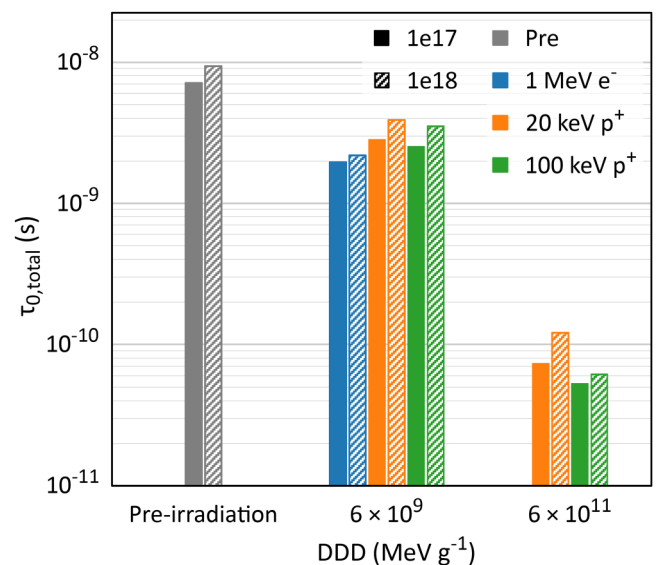


FIG. 10. The total lifetime ($\tau_{0,total}$) extracted from DIV fitting is plotted for 1×10^{17} and 1×10^{18} devices before irradiation, after irradiation with 1 MeV electrons to a DDD of 6×10^9 MeV g⁻¹ and after irradiation with 20 keV and 100 keV protons to DDDs of 6×10^9 and 6×10^{11} MeV g⁻¹.

23 June 2024 13:28:49

dark current–voltage curves calculated from the fitting model (TAT-SRH-A), using the fitting parameters in Table 1 of the [supplementary material](#). To simulate the case without TAT, Γ is simply set to 0, while all other parameters remain unaltered; i.e. model SRH-A is used.

The results of this test are summarized in [Fig. 11](#). This figure shows the V_{oc} ratio between devices irradiated to 6×10^9 and 6×10^{11} MeV g⁻¹ with 20 and 100 keV protons for 1×10^{17} and 1×10^{18} devices. This ratio is calculated for the experimental V_{oc} values, extracted from LIV data, and for the predicted V_{oc} values, with and without TAT. It can be seen that the TAT-SRH-A model predicts V_{oc} ratios that are very similar to the experimental data, with a maximum deviation of < 3 % of the model from the data, which is for the 100 keV proton-irradiated 1×10^{18} devices. The experimental and TAT-SRH-A data also show that the V_{oc} ratio is smaller for 1×10^{18} than for 1×10^{17} devices, as the former degrade more quickly. When TAT enhancement is removed from the model (SRH-A), the V_{oc} ratios increase, showing that TAT enhances the V_{oc} degradation rate. Furthermore, by removing TAT, the difference between the 1×10^{17} and 1×10^{18} ratios is reduced and the trend is reversed such that the ratio becomes greater for the 1×10^{18} devices. The difference between the models can be understood by considering that Γ , in Eqs. (5) and (6), acts as a multiplier for the carrier lifetime. Therefore, even with a similar decrease in the carrier lifetime for the 1×10^{17} and 1×10^{18} devices, the 1×10^{18} devices will experience a greater decrease in V_{oc} since their value of Γ at V_{oc} is greater due to the greater electric field across their absorber layers (see [Fig. 2](#)). In summary, [Fig. 11](#) demonstrates that the 1×10^{18} devices have a greater V_{oc} degradation rate than the 1×10^{17} devices because the electric field and resulting TAT

enhancement of the recombination rate are greater in the 1×10^{18} devices.

This differs from the explanations previously given for doping-based differences in radiation tolerance of thicker solar cells, which rely on the dominance of the diffusion current in these devices, or on the variation in the depletion region width with doping concentration.^{45–48} However, these explanations are not applicable to the UTSCs in this study, which are fully depleted, with the depletion region width effectively fixed at the absorber layer thickness, and for which the current–voltage behavior is dominated by the recombination–generation current. Conversely, the effect of TAT on the current–voltage behavior of thicker devices is expected to be small since it is limited to the depletion region, which tends to comprise a small fraction of the total active layer width of these devices.

2. Effect of radiation type

[Figure 11](#) also shows that the V_{oc} ratios are systematically smaller for 100 keV than 20 keV proton-irradiation. This reiterates the observation from [Fig. 5](#) that 100 keV protons cause a faster DDD-dependent V_{oc} degradation of the devices than 20 keV protons. In contrast to the doping dependence of radiation tolerance, significantly more relevant literature exists for the radiation type dependence. Many studies have compared the radiation damage induced by protons and electrons of various energies. DLTS data provide strong evidence for the theory that protons and electrons introduce different types of defects.^{31,32,41} These studies have also shown that radiation energy can affect the types of defects introduced as well as the relative introduction rate of different defects.^{32,49} Both of these factors will affect the rate of degradation of carrier lifetime and, therefore, V_{oc} . The relationship between carrier lifetime and defects is given by

$$\tau_0 = (k\sigma v \cdot \text{DDD})^{-1} = (K_{\tau, \text{DDD}} \cdot \text{DDD})^{-1}, \quad (10)$$

where k is the defect introduction rate, σ is the carrier capture cross section of a defect, and $K_{\tau, \text{DDD}}$ is the lifetime damage constant.

Therefore, if the difference in the V_{oc} degradation rate for 20 and 100 keV protons is due to a difference in the defect type or introduction rate, then this will be accompanied by a corresponding difference in the lifetime damage constant. The lifetime damage constants have been calculated for each device type irradiated with 20 and 100 keV protons and are tabulated in [Table V](#). $K_{\tau, \text{DDD}}$ was based on the total lifetimes ($\tau_{0, \text{total}}$ in Table 1 of the [supplementary](#)

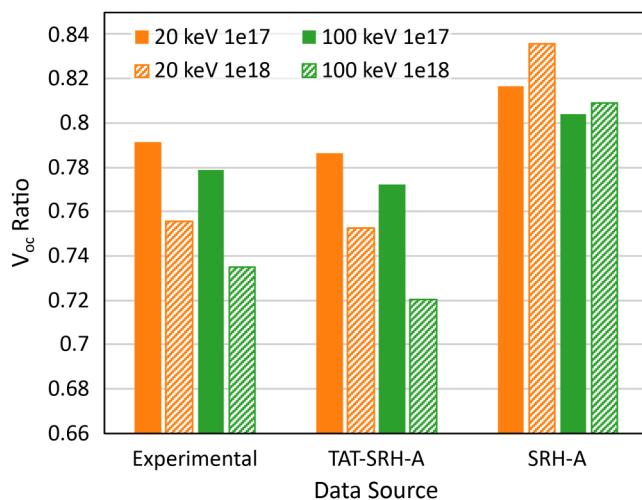


FIG. 11. The ratio between the V_{oc} of devices irradiated to DDDs of 6×10^9 and 6×10^{11} MeV g⁻¹ is plotted. A comparison is made between the ratios calculated from open-circuit voltages extracted from experimental LIV data and predicted by models including (TAT-SRH-A) and omitting (SRH-A) TAT enhancement. This is done for both 1×10^{17} and 1×10^{18} devices, irradiated with 20 and 100 keV protons.

TABLE V. Lifetime damage constants, in the DDD base. The constants are extracted from DIV fitting of 20 and 100 keV proton-irradiated devices.

Radiation type	Device type	$K_{\tau, \text{DDD}}$ (g MeV ⁻¹ s ⁻¹)
20 keV p ⁺	1×10^{17}	2.2×10^{-2}
	1×10^{18}	1.3×10^{-2}
100 keV p ⁺	1×10^{17}	3.1×10^{-2}
	1×10^{18}	2.7×10^{-2}

23 June 2024 13:28:49

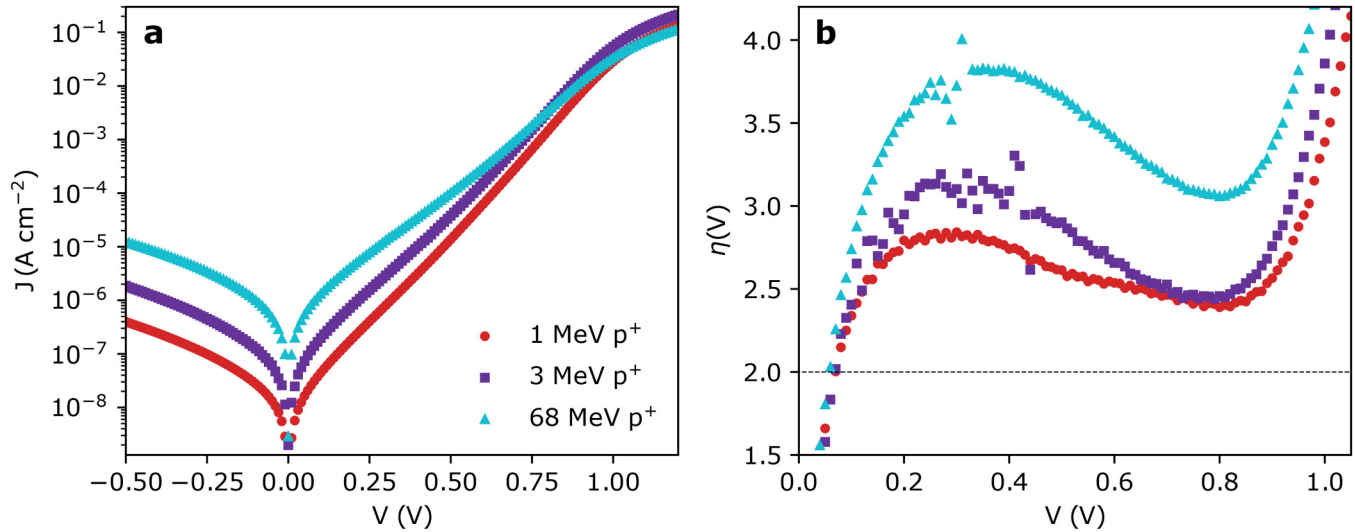


FIG. 12. (a) DIV and (b) a local ideality factor ($\eta(V)$) are plotted against voltage for 1, 3, and 68 MeV proton-irradiated 1×10^{18} UTSCs to DDDs of 6.1×10^9 , 5.3×10^9 , and 7.6×10^9 MeV g⁻¹, respectively.

material). Table V shows that, for each device type, $K_{\tau, \text{DDD}}$ is greater for irradiation with 100 keV protons than with 20 keV protons, which is in line with the greater V_{oc} degradation rate for 100 keV protons. This supports the idea that the radiation damage induced by protons is dependent on their energies and that 100 keV protons are more damaging per DDD than 20 keV protons because the defects produced by the former have either a greater capture cross section, a greater introduction rate, or a combination of both.

It is important to note, at this point, that this analysis could not be carried out for 1 MeV electrons and 1 MeV protons, as the DIV data for these could not be fitted to the same extent as for the low energy protons, or not at all. For the 1 MeV electrons, the DIVs for the devices irradiated to the lowest fluence could be fitted, but the fractional changes in lifetime and V_{oc} are much smaller for these fluences, leading to high fractional uncertainties. This is exacerbated by the low signal-to-noise ratio and influence of light biasing at low forward bias for the pre-irradiation and low dose DIV data.

C. Limitations of the model

Sections IV A and IV B demonstrated that the TAT-SRH-A carrier recombination model used in this study is able to fit much of the DIV data and explain trends in the radiation tolerance of the ultra-thin solar cells. However, it does have its limitations. Most notably, the model is unable to account for the very high ideality factors found in the 1 MeV proton-irradiated and high dose 1 MeV electron-irradiated devices, and as a result, good fits to their DIV curves could not be attained. Another limitation lies in the constraint of equal minority carrier lifetimes ($\tau_{n0} = \tau_{p0}$) that was applied in this study, which is discussed in Sec. III B 1 of the [supplementary material](#).

1. High ideality factors

In the case of the high dose, 1 MeV electron-irradiated devices, the difference between the local ideality factor of the data and the theoretical maximum of the model is only small, less than ~ 0.25 . This could be accounted for by an underestimation of the TAT enhancement factor, for example, due to a slight underestimation in the electric field or using values of effective mass, or intrinsic carrier concentration that deviate from the true value. However, in the case of the 1 MeV proton-irradiated devices, the model's underestimation of the data is more severe and the same explanation is less likely to be correct. Instead, it is likely that some further recombination mechanism, facilitated by the radiation damage caused by 1 MeV protons, must be considered to explain this behavior.

Further evidence supporting the hypothesis that high energy proton damage can facilitate a further recombination mechanism, given by DIV data from the same UTSCs irradiated with 3 and 68 MeV protons. These data, which are plotted in Fig. 12, have been drawn from previous studies^{2,50,51} and shows that the ideality factor of proton-irradiated devices, exposed to similar DDD, increases with proton energy.

A possible explanation for the very high ideality factors for high energy proton-irradiated devices is coupled defect recombination⁵² or deep donor-acceptor pair (DAP) recombination,^{53–55} which is a variant of the former. The DAP recombination mechanism has found success in describing the current-voltage behavior of mechanically damaged devices, for example, by cleaving, or scribing, where the mechanical damage has introduced localized regions of very high defect density. High energy proton radiation can also introduce extended regions of high defect density, which may similarly facilitate this mechanism.

23 June 2024 13:28:49

V. CONCLUSION

In this study, the open-circuit voltage degradation rate in the UTSCs was found to vary with both doping concentration in the absorber layer and radiation type (after accounting for differences in non-ionizing energy loss).

- (i) UTSCs with $1 \times 10^{18} \text{ cm}^{-3}$ doping concentration in their GaAs absorber layer degraded faster than those with $1 \times 10^{17} \text{ cm}^{-3}$.
- (ii) V_{oc} degradation rate increased with proton energy, from 20 keV to 1 MeV.
- (iii) V_{oc} degradation rate was less for 1 MeV electrons than for protons.

These trends were accompanied by the observation of significant variation in the DIV curves and associated local ideality factors of these devices with the same independent variables, as well as with radiation dose. Furthermore, values of ideality factor greater than 2 were observed.

The DIV data were fitted with a recombination model based on SRH recombination statistics, incorporating trap-assisted tunneling (TAT), using the formalism of Hurkx *et al.*³⁸ This demonstrated that

- (i) TAT causes elevated ideality factors.
- (ii) Incorporation of TAT in the model enabled accurate fitting of the DIV curves for devices pre-irradiation and after irradiation with 20 and 100 keV protons and low doses of 1 MeV electrons.
- (iii) The variation in the V_{oc} degradation rate with absorber layer doping concentration is a result of TAT enhancement of recombination rate, which is stronger in the more highly doped devices, where the maximum electric field is greater.
- (iv) The dependence of the V_{oc} degradation rate on the radiation type could be attributed to the dependence of the carrier lifetime degradation rate on the radiation type. This suggests that the capture cross sections of defects introduced by radiation, or the introduction rates of defects, or both, are dependent on the radiation type, in a way not accounted for by non-ionizing energy loss (NIEL) theory.

A shortcoming of the model is that it breaks down for devices irradiated with high energy protons ($>1 \text{ MeV}$), for which the ideality factors exceeded the maximum predicted by TAT. An increase in the ideality factor with proton energy was observed, and further work is required to understand this behavior.

The demonstration and theoretical understanding of the dependence of radiation tolerance on absorber layer doping concentration in the UTSCs will feed into further optimization of their design. Awareness of the dependence of the NIEL-corrected V_{oc} degradation rate on the radiation type is vital for future radiation testing of the UTSCs and predicting their longevity in space radiation environments.

SUPPLEMENTARY MATERIAL

See the [supplementary material](#) for supporting information, figures, tables, result, and discussion, as referenced in the main paper.

ACKNOWLEDGMENTS

This work was supported by the Royal Society (No. IEC\R3\193005), the H2020 European Research Council (No. 853365), and the UK Space Agency (No. PF2-012). A. Barthel acknowledges support from his EPSRC Ph.D. Studentship (No. EP/R513180/1).

AUTHOR DECLARATIONS

Conflict of Interest

The authors have no conflicts to disclose.

Author Contributions

A. Barthel: Conceptualization (equal); Data curation (equal); Formal analysis (equal); Investigation (equal); Methodology (equal); Visualization (equal); Writing – original draft (equal); Writing – review & editing (equal). **S.-I. Sato:** Investigation (equal); Methodology (equal); Resources (equal); Supervision (equal); Visualization (supporting); Writing – review & editing (equal). **L. Sayre:** Investigation (supporting); Methodology (equal); Writing – review & editing (supporting). **J. Li:** Investigation (supporting); Methodology (equal); Writing – review & editing (supporting). **T. Nakamura:** Investigation (equal); Methodology (equal); Resources (equal); Supervision (equal). **T. Ohshima:** Conceptualization (equal); Funding acquisition (equal); Project administration (equal); Resources (equal); Supervision (equal). **M. Imaizumi:** Conceptualization (equal); Funding acquisition (equal); Project administration (equal); Resources (equal); Supervision (equal). **L. C. Hirst:** Conceptualization (equal); Funding acquisition (equal); Methodology (equal); Project administration (equal); Resources (equal); Supervision (equal); Visualization (equal); Writing – review & editing (equal).

DATA AVAILABILITY

The data that support the findings of this study are available from the corresponding author upon reasonable request.

REFERENCES

- ¹L. C. Hirst, M. K. Yakes, J. H. Warner, M. F. Bennett, K. J. Schmieder, R. J. Walters, and P. P. Jenkins, "Intrinsic radiation tolerance of ultra-thin GaAs solar cells," *Appl. Phys. Lett.* **109**, 033908 (2016).
- ²A. Barthel, L. Sayre, G. Kusch, R. A. Oliver, and L. C. Hirst, "Radiation effects in ultra-thin GaAs solar cells," *J. Appl. Phys.* **132**, 184501 (2022).
- ³M. Imaizumi, T. Nakamura, T. Takamoto, T. Ohshima, and M. Tajima, "Radiation degradation characteristics of component subcells in inverted metamorphic triple-junction solar cells irradiated with electrons and protons," *Prog. Photovoltaics: Res. Appl.* **25**, 161–174 (2017).
- ⁴S.-I. Sato, H. Miyamoto, M. Imaizumi, K. Shimazaki, C. Morioka, K. Kawano, and T. Ohshima, "Degradation modeling of InGaP/GaAs/Ge triple-junction solar cells irradiated with various-energy protons," *Sol. Energy Mater. Sol. Cells* **93**, 768–773 (2009).
- ⁵C. Pellegrino, A. Gagliardi, and C. G. Zimmermann, "Difference in space-charge recombination of proton and electron irradiated GaAs solar cells," *Prog. Photovoltaics: Res. Appl.* **27**, 379–390 (2019).
- ⁶N. Gruginskij, F. Cappelluti, G. J. Bauhuis, P. Mulder, E. J. Haverkamp, E. Vlieg, and J. J. Schermer, "Electron radiation-induced degradation of GaAs

23 June 2024 13:28:49

solar cells with different architectures,” *Prog. Photovoltaics: Res. Appl.* **28**, 266–278 (2020).

⁷N. Gruginskie, F. Cappelluti, M. van Eerden, G. Bauhuis, P. Mulder, E. Vlieg, and J. Schermer, “Proton irradiation induced GaAs solar cell performance degradation simulations using a physics-based model,” *Sol. Energy Mater. Sol. Cells* **223**, 110971 (2021).

⁸N. Dharmarasu, A. Khan, M. Yamaguchi, T. Takamoto, T. Ohshima, H. Itoh, M. Imaizumi, and S. Matsuda, “Effects of proton irradiation on n-p InGaP solar cells,” *J. Appl. Phys.* **91**, 3306–3311 (2002).

⁹S. R. Messenger, G. P. Summers, E. A. Burke, R. J. Walters, and M. A. Xapsos, “Modeling solar cell degradation in space: A comparison of the NRL displacement damage dose and the JPL equivalent fluence approaches,” *Prog. Photovoltaics: Res. Appl.* **9**, 103–121 (2001).

¹⁰B. E. Anspaugh, *GaAs Solar Cell Radiation Handbook* (Jet Propulsion Laboratory, California Institute of Technology, Pasadena, CA, 1996), JPL publication No. 96-9.

¹¹H. Y. Tada, J. R. J. Carter, B. E. Anspaugh, and R. G. Downing, *Solar Cell Radiation Handbook*, 3rd ed. (Jet Propulsion Laboratory, California Institute of Technology, Pasadena, CA, 1982).

¹²X. J. Chen, H. J. Barnaby, J. H. Warner, S. R. Messenger, R. J. Walters, S. A. Ringel, and J. Park, “Non-linear behaviors of dark current slope in p⁺n GaAs solar cells following proton irradiations,” in *2009 34th IEEE Photovoltaic Specialists Conference (PVSC)* (IEEE, Philadelphia, PA, 2009), pp. 001565–001570.

¹³C.-T. Sah, R. Noyce, and W. Shockley, “Carrier generation and recombination in P-N junctions and P-N junction characteristics,” *Proc. IRE* **45**, 1228–1243 (1957).

¹⁴U. Aeberhard, “Nonequilibrium Green’s function picture of nonradiative recombination of the Shockley-Read-Hall type,” *Phys. Rev. B* **99**, 125302 (2019).

¹⁵J. Kim, Y. Tak, J. Kim, S. Chae, J.-Y. Kim, and Y. Park, “Analysis of forward tunneling current in InGaN/GaN multiple quantum well light-emitting diodes grown on Si (111) substrate,” *J. Appl. Phys.* **114**, 013101 (2013).

¹⁶M. Mandurrino, G. Verzellesi, M. Goano, M. Vallone, F. Bertazzi, G. Ghione, M. Meneghini, G. Meneghesso, and E. Zanoni, “Physics-based modeling and experimental implications of trap-assisted tunneling in InGaN/GaN light-emitting diodes: Physics-based modeling and experimental implications of TAT in InGaN/GaN LEDs,” *Phys. Status Solidi A* **212**, 947–953 (2015).

¹⁷D. Zhu, J. Xu, A. N. Noemaun, J. K. Kim, E. F. Schubert, M. H. Crawford, and D. D. Koleske, “The origin of the high diode-ideality factors in GaInN/GaN multiple quantum well light-emitting diodes,” *Appl. Phys. Lett.* **94**, 081113 (2009).

¹⁸H.-L. Chen, A. Cattoni, R. De Lépinay, A. W. Walker, O. Höhn, D. Lackner, G. Siefert, M. Faustini, N. Vandamme, J. Goffard, B. Behaghel, C. Dupuis, N. Bardou, F. Dimroth, and S. Collin, “A 19.9%-efficient ultrathin solar cell based on a 205-nm-thick GaAs absorber and a silver nanostructured back mirror,” *Nat. Energy* **4**, 761–767 (2019).

¹⁹S. I. Maximenko, M. P. Lumb, J. Moore, L. C. Hirst, M. K. Yakes, and P. P. Jenkins, “Thin GaAs solar cells for high irradiation levels,” in *2019 IEEE 46th Photovoltaic Specialists Conference (PVSC)* (IEEE, Chicago, IL, 2019), pp. 2814–2817.

²⁰I. Massiot, A. Cattoni, and S. Collin, “Progress and prospects for ultrathin solar cells,” *Nat. Energy* **5**, 959–972 (2020).

²¹G. Summers, E. Burke, M. Xapsos, C. Dale, P. Marshall, and E. Petersen, “Displacement damage in GaAs structures,” *IEEE Trans. Nucl. Sci.* **35**, 1221–1226 (1988).

²²G. P. Summers, E. A. Burke, and M. A. Xapsos, “Displacement damage analogs to ionizing radiation effects,” *Radiat. Meas.* **24**, 1–8 (1995).

²³G. Summers, E. Burke, P. Shapiro, S. Messenger, and R. Walters, “Damage correlations in semiconductors exposed to gamma, electron and proton radiations,” *IEEE Trans. Nucl. Sci.* **40**, 1372–1379 (1993).

²⁴L. Sayre, E. Camarillo Abad, P. Pearce, P. Chausse, P. Coulon, P. Shields, A. Johnson, and L. C. Hirst, “Ultra-thin GaAs solar cells with nanophotonic metal-dielectric diffraction gratings fabricated with displacement Talbot lithography,” *Prog. Photovoltaics* **30**, 96–108 (2022).

²⁵P. M. Pearce, E. Camarillo Abad, and L. C. Hirst, “Designing transparent nanophotonic gratings for ultra-thin solar cells,” *Opt. Express* **30**, 4528–4542 (2022).

²⁶E. Camarillo Abad, H. J. Joyce, and L. C. Hirst, “Transparent quasi-random structures for multimodal light trapping in ultrathin solar cells with broad engineering tolerance,” *ACS Photonics* **9**, 2724–2735 (2022).

²⁷D. Heynderickx, B. Quaghebeur, J. Wera, E. J. Daly, and H. R. D. Evans, “New radiation environment and effects models in the european space agency’s space environment information system (SPENVIS),” *Space Weather* **2**, S10S03 (2004).

²⁸E. El Allam, C. Inguibert, T. Nuns, A. Meulenberg, A. Jorio, and I. Zorkani, “Gamma and electron NIEL dependence of irradiated GaAs,” *IEEE Trans. Nucl. Sci.* **64**, 991–998 (2017).

²⁹F. Lei, R. Truscott, C. Dyer, B. Quaghebeur, D. Heynderickx, R. Nieminen, H. Evans, and E. Daly, “MULASSIS: A Geant4-based multilayered shielding simulation tool,” *IEEE Trans. Nucl. Sci.* **49**, 2788–2793 (2002).

³⁰D. Alonso-Álvarez, T. Wilson, P. Pearce, M. Führer, D. Farrell, and N. Ekins-Daukes, “Solcore: A multi-scale, Python-based library for modelling solar cells and semiconductor materials,” *J. Comput. Electron.* **17**, 1099–1123 (2018).

³¹J. H. Warner, C. D. Cress, S. R. Messenger, R. J. Walters, S. A. Ringel, and J. Park, “A deep level transient spectroscopy study of electron and proton irradiated p⁺n GaAs diodes,” *IEEE Trans. Nucl. Sci.* **57**, 1940–1945 (2010).

³²J. H. Warner, S. R. Messenger, R. J. Walters, G. P. Summers, M. J. Romero, and E. A. Burke, “Displacement damage evolution in GaAs following electron, proton and silicon ion irradiation,” *IEEE Trans. Nucl. Sci.* **54**, 1961–1968 (2007).

³³F. H. Eisen, K. Bachem, E. Klausman, K. Koehler, and R. Haddad, “Ion irradiation damage in n-type GaAs in comparison with its electron irradiation damage,” *J. Appl. Phys.* **72**, 5593–5601 (1992).

³⁴D. Stievenard, X. Boddaert, and J. C. Bourgoin, “Irradiation-induced defects in p-type GaAs,” *Phys. Rev. B* **34**, 4048–4058 (1986).

³⁵T. Yajima and L. Esaki, “Excess noise in narrow germanium P-N junctions,” *J. Phys. Soc. Jpn.* **13**, 1281–1287 (1958).

³⁶A. G. Chynoweth, W. L. Feldmann, and R. A. Logan, “Excess tunnel current in silicon Esaki junctions,” *Phys. Rev.* **121**, 684–694 (1961).

³⁷G. Hurkx, D. Klaassen, M. Knuvers, and F. O’Hara, “A new recombination model describing heavy-doping effects and low-temperature behaviour,” in *International Technical Digest on Electron Devices Meeting* (IEEE, Washington, DC, 1989), pp. 307–310.

³⁸G. Hurkx, D. Klaassen, and M. Knuvers, “A new recombination model for device simulation including tunneling,” *IEEE Trans. Electron Devices* **39**, 331–338 (1992).

³⁹K. Nordlund, J. Peltola, J. Nord, J. Keinonen, and R. S. Averback, “Defect clustering during ion irradiation of GaAs: Insight from molecular dynamics simulations,” *J. Appl. Phys.* **90**, 1710–1717 (2001).

⁴⁰J. H. Warner, C. Inguibert, M. E. Twigg, S. R. Messenger, R. J. Walters, M. J. Romero, and G. P. Summers, “Effect of proton and silicon ion irradiation on defect formation in GaAs,” *IEEE Trans. Nucl. Sci.* **55**, 3016–3024 (2008).

⁴¹C. Pellegrino, A. Gagliardi, and C. G. Zimmermann, “Defect spectroscopy and non-ionizing energy loss analysis of proton and electron irradiated p-type GaAs solar cells,” *J. Appl. Phys.* **128**, 195701 (2020).

⁴²A. Barry, A. Houdayer, P. Hinrichsen, W. Letourneau, and J. Vincent, “The energy dependence of lifetime damage constants in GaAs LEDs for 1–500 MeV protons,” *IEEE Trans. Nucl. Sci.* **42**, 2104–2107 (1995).

⁴³S. Khanna, S. Charbonneau, P. Piva, M. Parenteau, and C. Carlone, “Effects of 3 MeV proton irradiation on the excitonic lifetime in gallium arsenide,” *IEEE Trans. Nucl. Sci.* **45**, 2430–2435 (1998).

⁴⁴F. Lindholm, J. Fossum, and E. Burgess, “Application of the superposition principle to solar-cell analysis,” *IEEE Trans. Electron Devices* **26**, 165–171 (1979).

⁴⁵M. Yamaguchi and C. Uemura, “Changes in the electrical properties of GaAs due to electron irradiation,” *J. Appl. Phys.* **57**, 604–606 (1985).

⁴⁶D. Elfiky, M. Yamaguchi, T. Sasaki, T. Takamoto, C. Morioka, M. Imaizumi, T. Ohshima, S.-I. Sato, M. Elnawawy, T. Eldesuky, and A. Ghitass, “Effect of base doping concentration on radiation-resistance for GaAs sub-cells in InGaP/GaAs/Ge,” *Jpn. J. Appl. Phys.* **49**, 121202 (2010).

- ⁴⁷T. Takamoto, M. Kaneiwa, M. Imaizumi, and M. Yamaguchi, "InGaP/GaAs-based multijunction solar cells," *Prog. Photovoltaics: Res. Appl.* **13**, 495–511 (2005).
- ⁴⁸K. Bertness, B. Cavicchi, S. Kurtz, J. Olson, A. Kibbler, and C. Kramer, "Effect of base doping or radiation damage in GaAs single-junction solar cells," in *The Conference Record of the Twenty-Second IEEE Photovoltaic Specialists Conference—1991* (IEEE, Las Vegas, NV, 1991), pp. 1582–1587.
- ⁴⁹J. Warner, R. Walters, S. Messenger, G. Summers, S. Khanna, D. Estan, L. Erhardt, and A. Houdayer, "High-energy proton irradiation effects in GaAs devices," *IEEE Trans. Nucl. Sci.* **51**, 2887–2895 (2004).
- ⁵⁰A. Barthel, L. Sayre, F. Lang, G. Kusch, J. Bundesmann, A. Denker, R. Oliver, and L. Hirst, "Cathodoluminescence study of 68 MeV proton-irradiated ultra-thin GaAs solar cells," in *2020 47th IEEE Photovoltaic Specialists Conference (PVSC)* (IEEE, Calgary, AB, Canada, 2020), pp. 1070–1074.
- ⁵¹L. Sayre, F. Lang, J. Bundesmann, A. Denker, P. Pearce, A. Johnson, and L. Hirst, "Ultra-thin single-junction GaAs solar cells for extreme space environments," in *2020 47th IEEE Photovoltaic Specialists Conference (PVSC)* (IEEE, Calgary, AB, Canada, 2020), pp. 1621–1625.
- ⁵²A. Schenk and U. Krumbein, "Coupled defect-level recombination: Theory and application to anomalous diode characteristics," *J. Appl. Phys.* **78**, 3185–3192 (1995).
- ⁵³S. Steingrube, O. Breitenstein, K. Ramspeck, S. Glunz, A. Schenk, and P. P. Altermatt, "Explanation of commonly observed shunt currents in c-Si solar cells by means of recombination statistics beyond the Shockley-Read-Hall approximation," *J. Appl. Phys.* **110**, 014515 (2011).
- ⁵⁴O. Breitenstein, J. Bauer, A. Lotnyk, and J.-M. Wagner, "Defect induced non-ideal dark I-V characteristics of solar cells," *Superlattices Microstruct.* **45**, 182–189 (2009).
- ⁵⁵O. Breitenstein, P. Altermatt, K. Ramspeck, and A. Schenk, "The origin of ideality factors $n > 2$ of shunts and surfaces in the dark I-V curves of Si solar cells," in *21st European Photovoltaic Solar Energy Conference, Dresden*, September 2006 (WIP-Renewable Energies, Munich, 2006), pp. 626–628.